Cloud probability -based estimation of black-sky surface albedo from AVHRR data

Terhikki Manninen[1], Emmihenna Jääskeläinen[1], Niilo Siljamo[1], Aku Riihelä[1], Karl-Göran Karlsson[2]

[1]Meteorological research, Finnish Meteorological Institute, Helsinki, FI-00101, Finland
[2]Atmospheric Remote Sensing Unit, Research Department, Swedish Meteorological and Hydrological Institute, Norrköping, SE-60176 Norrköping, Sweden

Correspondence to: Terhikki Manninen (terhikki.manninen@fmi.fi)

Abstract. This paper describes a new method for cloud-correcting observations of black-sky surface albedo derived using the Advanced Very High Resolution Radiometer (AVHRR). Cloud cover constitutes a major challenge for the surface albedo estimation using AVHRR data for all possible conditions of cloud fraction and cloud type on any land cover type and solar zenith angle. This study shows how the new cloud probability (*CP*) data to be provided as part of the edition A3 of the CLARA (CM SAF cLoud, Albedo and surface Radiation dataset from AVHRR data) record by the project Satellite Application Facility on Climate Monitoring (CM SAF) of EUMETSAT can be used instead of traditional binary cloud masking to derive cloud-free monthly mean surface albedo estimates. Cloudy broadband albedo distributions were simulated first for theoretical cloud distributions and then using global cloud probability (*CP*) data of one month. A weighted mean approach based on the *CP* values was shown to produce very high accuracy black-sky surface albedo estimates for simulated data. The 90% quantile for the error was 1.1% (in absolute albedo percentage) and for the relative error it was 2.2%. AVHRR based and *in situ* albedo distributions were in line with each other and also the monthly mean values were consistent. Comparison with binary cloud masking indicated that the developed method improves cloud contamination removal.

1. Introduction

The surface albedo is a key indicator of climate change (GCOS, 2016) and is continuously and accurately measured across contrasting climatic zones by the Baseline Surface Radiation Network (BSRN), operated by the World Climate Research Programme (WCRP). However, satellite remotes sensing is required to augment these regional measurements with global estimates of surface albedo (König-Langlo et el., 2013; Driemel et al., 2018). Remote sensing is the only reasonable alternative for augmenting regional surface albedo estimates globally. EUMETSAT provides the climate community with satellite based surface albedo products in the project CM SAF, which is part of the EUMETSAT Applications Ground Segment (Schulz et al., 2009). The CLARA data record contains cloud properties, surface albedo and surface radiation parameters derived from the AVHRR sensor onboard polar orbiting NOAA and METOP satellites. The CLARA-A2 (second edition) covered the years 1982-2015 and the next edition, A3, will cover the years 1979 – 2020.

The determination of surface black-sky albedo (Lucht et al. 2000, Román et al., 2010) from satellite data is usually carried out after first applying a cloud masking procedure. Thus, the accuracy of the cloud mask is really crucial to the albedo product. In spite of augmenting information of global reanalysis data from ERA-5 (Hersbach et al., 2020), land mask and topography data, the demand of high accuracy pixelwise cloud masking of AVHRR images in all possible cloud fraction and type situations is

5   extremely challenging, especially for the oldest satellites, due to lack of one of the two split-window infrared channels at 12 micron wavelength, and the high and variable noise levels in the 3.7 micron channel. Earlier comparisons of AVHRR cloud masks with Moderate Resolution Imaging Spectroradiometer (MODIS) based cloud masks estimated that 1 – 3 % of the nominally clear local area coverage AVHRR data are cloud contaminated (Heidinger et al., 2002). More recent studies making use of high sensitivity lidar measurements from the Cloud-Aerosol Lidar and Infrared Pathfinder Satellite Observation

10   (CALIPSO) mission indicate that the fraction of missed clouds is significantly higher and may even exceed 10 % in some geographical regions (Karlsson et al., 2017 and Karlsson and Håkansson, 2018). One factor that explains this difference to earlier studies is that the CALIPSO-CALIOP lidar is able to observe also very thin clouds which are truly non-visible to AVHRR data. However, for the really large deviations also other cloudy vs clear non-separability issues become important. For example, low-level clouds being in shadow at high solar zenith angles (e.g., caused by higher level clouds or mountain

15   peaks) might be missed as a consequence of having non-typical visible and NIR reflectances as well as a lacking temperature difference between the cloud top and the surface. If such missed clouds occur over snow-covered surfaces, they might lead to a seriously underestimated surface albedo. Using such data would introduce errors on the order of 100% on derived surface albedo, with potentially much higher errors occurring in cases with the combination of snow, complex terrain and low sun elevation, which are common in Northern Europe for example. For this reason, the surface albedo of the CLARA surface

20   albedo product is restricted to limited to cases, for which the solar zenith angle $\leq 70°$.

Another approach to tackle cloudy conditions has been developed in this study. It appears that clear (or almost clear) sky and completely cloudy sky situations are much more frequent than the intermediate conditions (Manninen et al., 2004). Due to the great variation of cloud properties also the cloud albedo varies considerably. Thus, across a 0.25 x 0.25 degree grid-box over

25   one month, the slowly varying surface albedo would be expected to dominate the broadband albedo distribution observed by non-cloud masked AVHRR data. The CLARA-A3 data record of CM SAF will provide the cloud probability as a new product. Here a method for estimating the surface albedo from the cloudy albedo distribution using the cloud probability values is presented. Theoretical simulations provide the basis for formulas used for estimating the cloud-free albedo distribution peak value without the need to construct the distribution itself, thus shrinking markedly the need of computer resources. The results

30   are compared with in situ measurements at snow-free and snow-covered test sites.

The *in situ* albedo data used for validation of the satellite based albedo estimates are presented in Section 2.1. The satellite data used is described in Section 2.2 with emphasis on the atmospheric correction (Section 2.2.2) and the cloud probabilities (Section 2.2.3). The method how to take cloudiness into account when estimating the surface albedo is described in Section 3.

The essential points of a previous theoretical study (Manninen et al., 2004) of deriving cloudy albedo distributions are summarized in Section 3.1.1. Then the approach is further developed to adapt it to simulations based on satellite based cloud probability data (Section 3.1.2) and finally a new method how to derive the cloud-free surface albedo using cloud probabilities is presented (Section 3.2).

2. Materials

2.1. *In situ* albedo data

To verify the satellite-based albedo estimates, in situ surface albedo measurements were obtained from a selection of sites in the Baseline Surface Radiation Network (BSRN; Driemel et al., 2018). The sites Desert Rock (DRA), Southern Great Plains (E13), Payerne (PAY), Fort Peck (FPE), Cabauw (CAB), Syowa (SYO), and Neumayer (GVN) were selected for their combination of albedo measurement availability with acceptable spatial representativeness of the site's measurement with respect to the albedo of the surrounding area, which is an important aspect for the point-to-pixel comparisons of satellite observations with in situ measurements. The BSRN measurements are quality-monitored and the instruments regularly maintained, ensuring good quality as a reference dataset.

Additionally, data from the Summit Camp site of the Greenland Climate Network (Steffen et al., 1996) was used to add coverage over ice sheet snow cover; the Summit site is often used as a snow albedo validation site for satellite studies due to the relatively low heterogeneity of the surface albedo in the area around the site.

2.2. AVHRR data

2.2.1. Fundamental Data Record (FDR)

The used AVHRR radiance data record is defined by applying the PyGAC preprocessing tool (Devasthale et al., 2017, https://pygac.readthedocs.io/en/develop/) to the original AVHRR L1b data record hosted by NOAA. For the visible AVHRR channels PyGAC is using an updated calibration method originally formulated by Heidinger et al. (2010). Applicable calibration coefficients are described by the PyGAC documentation and they are based on the NOAA PATMOS-x calibration information published at https://cimss.ssec.wisc.edu/patmosx/avhrr_cal.html with its latest update in 2017. This data record has still not full Fundamental Climate Data Record (FCDR) status since the infrared channel radiances are not fully intercalibrated in the same way as the visible channels. Consequently, the entire AVHRR data record will be published by EUMETSAT in 2022 as being a FDR while a data record with full FCDR status is planned for release in 2026.

2.2.2. Atmospheric correction

To achieve black-sky surface albedo (SAL) from the Top-Of-Atmosphere (TOA) reflectances, the atmospheric effects need to be removed. In processing of CLARA-A3 SAL this is done using the Simplified Method for Atmospheric Corrections (SMAC, Rahman, H. and Dedieu, G., 1994) algorithm. The SMAC algorithm reduces the TOA reflectances to surface reflectances. In addition to TOA reflectances (as an output from Polar Platform Systems (PPS) pre-processing step), the SMAC algorithm needs other atmospheric input parameters (ozone content, surface pressure, total column water vapour content and aerosol optical depth (AOD) at 550 nm). For CLARA-A3 SAL, surface pressure, ozone content, and water vapour content are derived from ECWMF ERA5 global reanalysis data. The AOD at 550 nm are from the AOD time series by Jääskeläinen et al. (2017). It is based on the Total Ozone Mapping Spectrometer (TOMS) and Ozone monitoring instrument (OMI) Aerosol Index (AI) data. Only AOD smaller than unity are used for SAL retrieval. For sea and permanent ice areas the constant AOD value 0.05 is used.

2.2.3. Cloud probabilities

The new surface albedo retrieval approach makes use of some recent cloud masking developments taking place in the EUMETSAT Nowcasting Satellite Application Facility (NWC SAF) project. The NWC SAF cloud processing package PPS (Polar Platform System) has for many years provided cloud masks based on an original multispectral thresholding algorithm first described by Dybbroe et al., (2005). However, the latest version of PPS (denoted PPS version 2018) has added a complementary cloud masking method capable of providing cloud probabilities instead of fixed binary cloud masks as output. This product, denoted CMA-prob, is based on Bayesian retrieval theory and a first prototype method was described by Karlsson et al. (2015). A substantially upgraded version, applied to both AVHRR and Spinning Enhanced Visible and InfraRed Imager (SEVIRI) data, was presented in Karlsson et a. (2020) and is now officially added to PPS version 2018. Results from this particular CMA-prob version have been utilised in this study.

The original cloud probability CP values of CMA-prob per orbit in Global Area Coverage GAC resolution (~5 km) globally for June 2012 were used as the starting point. Since the Surface Albedo Product (SAL) is delivered in a global grid of 1440 x 720 pixels, the pixelwise monthly distributions of CP values were generated in that resolution. CP values for cases where the solar zenith angle exceeds 70° were discarded for consistency with the same constraint in albedo calculations. Pixelwise distributions of CP (altogether 31020) were calculated for every 5th pixel for the whole area, which naturally covered more the Northern Hemisphere due to illumination requirements. Examples of them are shown in Figure 1. for the 10 largest pixelwise sets and the mean of all distributions. Obviously, very small cloud probability is more common than about 20%. The number or individual CP values per distribution was on the average 1777, the 80% variation range being 203 – 2291. The number of CP values in the 10 largest distributions varied in the range 4064 – 4327.

The satellite based *CP* values provided by the PPS software in GAC resolution are used in Section 3.1.2 as the basis for simulations of the effect of cloud fraction on the surface albedo. The *CP* is taken to statistically represent the cloud fraction and only values smaller than 20% were used in this study, in order to achieve high accuracy for the surface albedo estimate. In principle, a *CP* value of 50 % could be suggested at first sight, but it would then mean that a fairly high risk remains that a truly cloudy pixel could be mistaken for being cloud-free. In addition, the cloud probability is also linked to clouds' optical thicknesses meaning that optically thick clouds are easier to detect than thinner clouds (thus, having higher *CP* values). Thus, to reduce the risk of mistaking clouds with relatively high optical thicknesses for being cloud-free, a lower *CP* threshold should therefore be used. A reasonable value that reduces this risk of misclassification, but which still allows a large enough sample of cloud-free cases is found at a *CP* value of 20 %. As the data mass even for every 5th pixel is quite large (620400 individual *CP* values), the data was still reduced for the simulations the following way. First the ten largest distributions were taken, because they are statistically representative. Then every 50th set in decreasing order of the number of points in the distribution. Altogether 612 *CP* distributions was used in the simulations. The reason to use also very small distributions (the smallest set had only 14 *CP* values) in the simulations was that such cases appear also, when deriving monthly albedo means using satellite data. For this data, the cloud probability did not mostly correlate with the solar zenith or azimuth angle. Hence, the simulations can be carried out combining any *CP* values to any surface albedo values without paying attention to the solar angles. Further on, as the SAL product currently is not normalized to any specific solar zenith angle, the results of Section 3.1 can be applied to SAL processing without further consideration of solar angle effects on the results.

3. Methods

The cloud-free surface albedo estimates of CLARA-A3 will be estimated using the TOA reflectance and *CP* values available in pixel basis (Figure 2). First the TOA reflectance values with *CP* > 20% are discarded, as well as values flagged as low quality by the PPS software, for example because of sun glints. Then the atmospheric correction is carried out the same way for all remaining TOA reflectances independently of the cloud probability. Finally, the monthly mean cloud-free surface albedo is estimated using the atmospherically corrected reflectances and corresponding *CP* values. The main points of the theoretical background for the cloudy surface albedo distributions (Manninen et al., 2004) are summarized in Section 3.1.1. The adaptation of the theoretical approach to using cloud probability data is described in Section 3.1.2 and finally the formulas for deriving the cloud-free monthly mean surface albedo estimates are provided in Section 3.2.

3.1. Simulation of cloudy surface albedo distributions

3.1.1. Theoretical cloud distributions

The cloud fraction varies between the two extremes, zero and unity, with varying weather conditions. When estimating the cloud fraction distribution over the entire globe in a very coarse spatial resolution, however, it is possible that the extreme values are not achieved at all. The ultimate limit is the planetary cloudiness, which is on the average about 66 % according to

5

the latest report from the Global Energy and Water Exchanges GEWEX cloud assessment study (Stubenrauch et al 2021), the annual variation being about ± 5% (Karlsson and Devasthale, 2018). On the other hand, in very high spatial resolution the cloud fraction is typically clearly dominated by the extreme values, as is shown by ceilometer observations, for example (Manninen et al., 2004). Although the cloud probability estimation is complicated by various kinds of uncertainties, the observed cloud fractions based on AVHRR data showed a U-curve resembling distribution both in original 1.1 km (Manninen et al., 2004) and the GAC resolution of ~5 km. The median and 80% variation range of the relative *CP* distributions are shown in Figure 1 for every 5th *CP* (and SAL) end product pixel (0.25° x 0.25°) available globally in June 2012. The leftmost part of the U-curve is shown for a few individual example end product pixels. Thus, it is more common to have completely cloud-free and completely cloudy pixels, but all intermediate values are also possible. A functional dependence adequate for fitting the observed cloud fraction curves seems to be (Manninen et al., 2004)

$$f_k(k) = exp(-ck) + b \, exp(-c(100 - k)) \tag{1}$$

where k is the cloud cover percentage and b and c are parameters depending on the spatial resolution.

The sun elevation dominates the diurnal variation of surface black-sky albedo (Briegleb and Ramanathan, 1982; Briegleb et al, 1986; Yang et al., 2008; Manninen et al., 2020). The diurnal albedo distribution is in snow-free areas almost symmetric, when the surface albedo is normalized with respect to midday, although the albedo is typically slightly lower in the morning than in the afternoon for the same solar zenith angle due to the presence of dew (Mayor et al., 1996). For snow cover during the melting season the albedo tends to be almost linearly decreasing during the day (Pirazzini 2004; Manninen et al., 2020; Manninen et al., 2021). In addition, the seasonal variation within one month may cause slight skewness in the albedo distribution.

The albedo of the surface and clouds should dominate the albedo distribution, because perfectly cloudy and perfectly clear skies are much more common than intermediate cloudiness. As long as the land use class does not change, the snow-free surface albedo has typically only moderate seasonal variation, but the albedo of clouds varies in a wide range with varying cloud type (Brisson et al., 1999). Therefore the monthly albedo distribution of a snow-free surface constitutes usually only one distinct peak, which is located roughly at the surface albedo value. This is the case also for snow cover in midwinter conditions, but during the melting season the distribution is much broader (Manninen et al., 2019). However, a Gaussian monthly albedo distribution *f(α)* is a reasonable approximation for both snow-free and snow-covered surfaces, i.e.

$$f(\alpha) = \int_{x=0}^{100} exp\left(-\frac{(x-\bar{x})^2}{2\sigma_x^2}\right) dx \tag{2}$$

where $\bar{x}$ is the surface albedo average, σ_x is the standard deviation of the surface albedo distribution and α denotes the albedo variable. The monthly albedo distribution observed by optical satellite radiometers can be described as a combination of the

surface albedo distribution, the cloud coverage distribution and cloud shadow distribution (Manninen et al., 2004). The surface albedo distribution normalized with respect to midday is typically reasonably close to Gaussian distribution. In high resolution (50m) the cloud albedo has been observed to represent the Weibull distribution (Koren and Joseph, 2000). In GAC resolution, a pixel may contain several layers of diverse cloud types and the time window for the distribution is one month. Consequently, the albedo distribution of cloudy pixels is then a random combination of single cloud type distributions. Hence, the cloud albedo distribution in GAC resolution can be assumed to be Gaussian, although the standard deviation may be so large, that the result is essentially the same as for uniform distribution. No actual distribution shape is motivated for shadows, because their existence requires several conditions to apply simultaneously: 1) the pixel in question must be clear, 2) there must be a cloud close enough in the neighbourhood 3) the Sun elevation and azimuth angles must be such that the Sun is on the same line with the pixel in question and the cloud casting the shadow. Since slightly shadowed pixels are more probable than completely shadowed pixels an exponentially decaying distribution was assumed for shadows according to

$$f_p(p) = \exp(-10p) \tag{3}$$

where p is a uniform random variable in the range [0, 1]. Then the probability density function (PDF) f_s of the possibly shaded pixels is defined as an integral of the product of the individual PDFs of the shadow p and the surface albedo value x. The Kronecker delta function (δ) is included in the integral to restrict the integration to possible combinations of α, p and x and to include only cases with the cloud fraction $k = 0$ so that (Manninen et al., 2004) the probability density function f_s for possibly shaded cloud-free pixels is

$$f_s(\alpha) = \int_{x=0}^{100} \int_{p=0}^{1} exp\left(-\frac{(x-\bar{x})^2}{2\sigma_x^2}\right) \, exp(-10p) \, \delta\left(\alpha - x\,(1-p) + \frac{x}{2}p\right) \, \delta(k) \, dxdp \tag{4}$$

assuming that the lowest albedo value that will be caused by shadowing is half of the true value. This assumption was based on empirical observations using AVHRR data (Manninen et al., 2004).

The theoretical monthly albedo probability density function of cloudy pixels $f_c(\alpha)$ is likewise defined as an integral of the product of the individual PDFs of the cloud fraction k (given here in percentage), cloud albedo value y, and the surface albedo value x. Again the Kronecker delta function is included in the integral to restrict the integration to possible combinations of α, k, x and y so that

$$f_c(\alpha) = \int_{x=0}^{100} \int_{y=0}^{100} \int_{k=0}^{100} exp\left(-\frac{(x-\bar{x})^2}{2\sigma_x^2}\right) exp\left(-\frac{(y-\bar{y})^2}{2\sigma_y^2}\right) \left(exp(-c\,k) + b\,exp(-c(100-k))\right) \delta\left(\alpha - \frac{(100-k)x + k\,y}{100}\right) \, dxdydk \tag{5}$$

where $\bar{y}$ is the cloud albedo average and σ_y is the standard deviation of the cloud albedo. The cloud albedo distribution is here assumed to be Gaussian, but sometimes the standard deviation is so large, that the result is essentially the same as for a uniform distribution. The total PDF $f_t(\alpha)$ covering all cases is

$$5 \quad f_t(\alpha) = \begin{cases} f_s(\alpha), & k = 0 \\ f_c(\alpha), & k > 0 \end{cases} \quad\quad\quad (6)$$

The location of the local maxima (and minima) of the albedo distributions of Eqs. 4 and 5 correspond to albedo values α for which $f_t{}'(\alpha) = 0$. Since the integrals can't be determined in closed form, no explicit relationship between the peaks of the PDF of the true surface albedo $f(x)$ and the PDF of the total albedo $f_t(\alpha)$ can be derived. Thus the albedo PDFs are simulated
10   numerically.

For cloud-free cases the average surface albedo value of an experimental albedo distribution can be determined as the mean of the upper and lower half height locations of the albedo distribution (Manninen et al., 2004). For the theoretical Gaussian distribution this equals the mean value precisely. For cloudy cases the total albedo distribution is mostly not symmetric and
15   using the mean of the lower and upper half height albedo values results in overestimation of low surface albedo and underestimation of high surface albedo mean values. It is not possible to derive a functional relationship in closed form between the clear sky and cloudy albedo means even for theoretical distributions. In addition, the cloud fraction and type vary in large ranges, so that nothing can be assumed concerning the shape of the cloudy albedo peak. It may be distinctly skewed or almost symmetric. It may dominate the whole distribution or the background may be at the half height level of the peak. Therefore
20   robust parameters assuming nothing of the shape of the peak are sought for determining the mean surface albedo.

In a previous study the half-height width and the ¾ height width of the cloudy albedo distribution peak was shown to be suitable for the true albedo value determination (Manninen et al., 2004). However, constructing distributions and determining the peak widths is numerically a very slow process. This is not feasible when processing a long times series (~ 40 years)
25   globally (1440 x 720 pixels) even on monthly basis. Therefore, in this study we present a solution to estimate the surface albedo peak value without the need to construct the distribution. It is derived by simulations of cloudy albedo distributions based on observed statistics of the newly available cloud probability values (see Section 3.1.2).

3.1.2. Satellite based cloud distributions

The satellite based cloud probability data provided by the PPS software (Karlsson et al., 2020) were used as proxies for cloud
30   fractions. The total albedo distributions were calculated separately for each pixelwise CP distribution $f_{CP}(CP)$. Thus, the

equations to use for satellite based versions of the cloud-free, but possibly shaded, pixel distribution f_s and cloudy pixel distribution f_c, f_{Ss} and f_{Sc} respectively, for each individual pixelwise cloud probability distribution are now

$$f_{Ss}(\alpha) = f_{CP}(0) \int_{x=0}^{100} exp\left(-\frac{(x-\bar{x})^2}{2\sigma_x^2}\right) \; exp(-10p) \; \delta\left(\alpha - x\,(1-p) + \frac{x}{2}p\right) \; dx \tag{7}$$

$$f_{Sc}(\alpha) = \sum_{k=1}^{19} f_{CP}(k)\, exp(-d\,k) \int_{x=0}^{100} exp\left(-\frac{(x-\bar{x})^2}{2\sigma_x^2}\right) dx \qquad , \tag{8}$$

where k is the cloud probability discretized to integers in the range [1,19], because only CP values smaller than 20% are allowed in order to achieve high estimation accuracy. As larger CP values than that are not used in the analysis, it is sufficient to replace the term $exp\,(-c\,k) + b\,exp\,(-c\,(100 - k))$ of Eq. 5 by $exp(-d\,k)$. The parameter $d = 0.1$ is used to give even more weight for less cloudy albedo retrievals yet allowing some weight (0.135) also to the 20% cloud probability cases. The choice of the value of d is a compromise between theoretical accuracy and desire to avoid dominance of individual completely cloud-free retrievals. The reason not to integrate Eq. 7 over the parameter p like in Eq. 4 is purely practical: the data mass is too large for that. Hence, just one random shadow value is taken into account per a CP. Each cloud probability distribution is combined with different values of the surface albedo distribution using random weights to improve the generalization of the results, as satellites observe samples of the surface albedo distribution in varying cloud conditions. The total albedo distribution $f_{St}(\alpha)$ is then derived as a combination of those two alternatives as before using Eq. 6, where f_t, f_s and f_c are replaced by f_{St}, f_{Ss} and f_{Sc} respectively. The first estimate of the surface albedo mean $\bar{\alpha}$ is then obtained from n individual albedo values as follows

$$\bar{\alpha} = \sum_{i=1}^{n} \alpha_i\, f_{St}(\alpha_i) / \sum_{i=1}^{n} f_{St}(\alpha_i) \tag{9}$$

The monthly standard deviation, skewness and kurtosis are then calculated similarly using the total albedo distribution as weights. When a sufficient number of cloud-free pixels is present, this formula will give a good estimate for the surface albedo. However, if all pixels have 20% probability, the above formula will approach the albedo value corresponding to 20% cloud probability, not 0% cloud probability. Hence, an additional correction terms is applied to retrieve the final albedo estimate $\hat{\alpha}$ in the form

$$\hat{\alpha} = \bar{\alpha}\left(1 + c_1 \overline{CP} - \frac{c_2\, \overline{CP}}{\bar{\alpha}}\right) \tag{10}$$

where $\overline{CP}$ is the monthly mean cloud probability of the CP values within the range [0%, 20%) and c_1 and c_2 parameters are determined empirically on the basis of the simulations. The assumed cloud albedo mean and standard deviation were 60% and 20%, respectively, and the calculations were made for Gaussian surface albedo with mean values 10%, 20%, 30%, 40%, 50%, 60%, 70% and 80% and with a standard deviation of 2%. The values of c_1 and c_2 producing the best fit of estimated albedos

to the true ones are given in Table 1. This formula adjusts the albedo estimate only, when $\overline{CP}$ exceeds zero. The standard deviation, skewness and kurtosis estimates based on $\bar{\alpha}$ are corrected similarly using the correction factor in brackets of Eq. 10, but with the dedicated parameter values of c_1 and c_2 given in Table 1.

3.2. Surface albedo retrieval algorithm

5   The surface albedo algorithm used in the Climate-SAF project starts with atmospheric correction carried out using the SMAC method (Rahman and Dedieu, 1994: Proud et al, 2010). The next step is to determine the albedo values for the visible and near infrared channels with the generally used formulas and coefficients for BRDF of various land use classes, which are taken from a land cover product (Roujean et al., 1992; Wu et al., 1995; Hansen et al., 2000). A topography correction is carried out in mountainous areas (Manninen et al., 2011). Finally, a broad band conversion is carried out (Liang, 2000; Liang et al., 2002).

10   Currently, no solar zenith angle normalization is used, because at the time of the product development no generally applicable formula existed for all surface types, including melting snow (Manninen et al., 2020). The previous SAL versions (Riihelä et al. 2013, Karlsson et al., 2017; Anttila et al. 2018) relied on cloud masking applying the SAL algorithm only on nominated clear-sky pixels.

15   For the next release, CLARA-A3 SAL, the cloud probability values *CP* provided by the PPS software (Karlsson et al., 2020) will be available and the black-sky surface albedo (Lucht et al., 2000; Róman et al., 2010) retrieval will be based on pixels with cloud probability not exceeding 20 %. The albedo processing is first carried out as if all those pixels were completely cloud-free, i.e. the atmospheric correction for AOD, water vapour, air mass, and ozone is made. Then the monthly mean values $\bar{\alpha}$ are approximated similarly as in Section 3.1.2

20

$$\bar{\alpha} = \sum_{i=1}^{n} \alpha_i \exp(-d\, CP_i) / \sum_{i=1}^{n} \exp(-d\, CP_i) \tag{11}$$

The theoretically motivated form of Eq. 10 for correcting $\bar{\alpha}$ turned out to result in slight black-sky albedo overestimation for large, especially sea ice, albedo values, when comparing to previous albedo time series. Since Eq. 11 is not a precise theoretical

25   formula for deriving the cloud-free albedo using possibly cloudy data, but rather a practical statistical approach for its estimation, it is understandable that a theoretical correction factor form may not be optimal either. Thus, finally an ordinary linear regression based empirical correction of $\bar{\alpha}$ was derived using the albedo simulations (Section 3.1.2). Hence, the final monthly mean albedo estimates $\hat{\alpha}$ were derived instead of Eq. 10 using the following formula

30    $$\hat{\alpha} = 1.0332\, \bar{\alpha} - \overline{CP}(-0.05600 + 0.007026\, \bar{\alpha}) \qquad . \tag{12}$$

The difference between $\hat{\alpha}$ and $\bar{\alpha}$ is rather small and consequently the standard deviation, skewness and kurtosis were still corrected using Eq. 10.

4. Results

4.1. Simulated distributions

5 Albedo distributions were simulated for surfaces with Gaussian mean albedo values 10%, 20%, 30%, 40%, 50%, 60%, 70% and 80% and a standard deviation of 2%. The Gaussian cloud albedo mean was taken to be 60% with a standard deviation of 20%. Examples of them are shown in Figure 3. For convenience all distributions are scaled so that the maximum equals unity instead of using the common normalization of PDFs which would set the integral to unity and consequently cause varying peak height. Obviously, for relatively low surface albedo values (such as those of vegetation) the clouds cause a tail at the high

10 end of the albedo distribution and for high albedo values (such as those of snow) a tail at the low end. For albedo values close to the cloud albedo (such as sea ice albedo values) the distribution spreads both to low and high values. The bump at the cloud albedo mean is more distinct for high large b and c of Eq. 5. Due to the larger standard deviation of the cloud albedo distribution and the variation of the cloud probability, the surface albedo distribution peak still dominates the total distribution.

15 Albedo distributions were also derived using the empirical *CP* pixelwise distributions and Eqs. 11 and 10. The results were compared with the true values (Table 2). For the simulated Gaussian albedo distributions the obtained estimation accuracy is very good: the mean absolute difference is 0.48% and the 90% quantile for the mean value is 1.1% (in absolute albedo percentage). The relative mean albedo difference is 1.1% and the 90% quantile for the relative difference is 2.2%. But also larger deviations appear: the maximum mean albedo error is 2.8% (in absolute percentage) and the relative mean albedo error

20 is 7.8%. The effect of the number of individual points in the simulation on the accuracy and relative accuracy of the albedo estimation is shown in Figure 4. Naturally, large number of points increases the accuracy, but the effect is not dramatic. This is important from the point of view of satellite images, because the number of individual points for a monthly mean may be quite small in areas, where the sun elevation is typically small or the sky cloudy.

25 The reason for the very high accuracy is partly due to the assumed purely Gaussian surface albedo distributions that are provided for the whole range [0%, 100%] with an increment of 1%. For satellite data the surface albedo distributions are patchy and the sampling may be biased to certain solar zenith angle values. In addition, the distributions may deviate clearly from Gaussian. Moreover, the number of individual satellite based albedo estimates per pixel may be much smaller than the 101 used in these simulations. Hence, it is not expected to achieve this high accuracy for the satellite based albedo estimates, but

30 in principle this approach is capable of achieving very high albedo estimation accuracy.

4.2. Satellite based distributions

Histograms of surface albedos in GAC resolution for one month were constructed using the new CLARA-A3 SAL algorithm for the chosen relatively homogeneous test sites Desert Rock (36.626°N, 116.018°W), Payerne (46.815°N, 6.944°E), Southern Great Plains (36.605°N, 97.485°W) and Greenland Summit (72.580°N, 38.500°W) with 1% bin width (Figure 5). The corresponding *in situ* albedo distributions are shown as well. Only those points are shown for which both a satellite overpass and an *in situ* measurement were available within a 15 minute time window. Monthly means derived from simultaneous *in* situ and satellite based albedo values are given for several site in Table 3. Since the irradiance of the *in situ* measurements also contains contribution from the atmosphere, the comparison to a black-sky surface albedo estimate contains some inherent discrepancy, but for dark surfaces the *in situ* albedo values should be only slightly larger than the satellite based values. The difference increases with increasing AOD due to resulting increase of atmospheric scattering, the role of which is the more marked the lower is the surface scattering. For bright targets, such as snow, the effect of the atmosphere reduces the measured surface albedo value, because the target is so highly scattering that the increase of atmospheric scattering due to AOD is smaller than the reduce of target scattering due to smaller amount of irradiance reaching the surface. In addition, the satellite pixel diameter is about 25 km and the *in situ* measurements typically characterize footprints of some hundreds of square meters. Possible land cover inhomogeneity around the measurement site inevitably causes discrepancy between the satellite and *in situ* values (Riihelä et al., 2013). The difference between *in situ* and satellite based values is typically largest in winter conditions (November), when occasional snow falls may increase the *in situ* albedo markedly, whereas the satellite detects still large snow-free dark targets, such as Lac Neuchâtel in Payerne, or the scenery, like in Fort Peck, contains coniferous forests, which are mostly relatively dark even in snow covered conditions. The reason for the high *in situ* albedo of Cabauw as compared to the satellite based albedo is related to the typically thick atmosphere of Cabauw. The difference between the albedo means shows slight increase with decreasing number of individual values behind the means and increasing distance between the mean of the satellite pixel locations and the measurement point.

In sea ice areas the variation of the surface albedo within one month may be large due to large amounts of open water and movement of the ice field. Examples of that are shown in Figure 6 for sites in Arctic Ocean of Alaska, Kara Sea and Laptev Sea. In 2009 there was in June still quite a lot of sea ice in all those three areas, whereas in June 2018, due to the climate change, all of those sites were relatively ice free, especially Laptev sea having a large area of open water (EUMETSAT, 2021). When the sea ice concentration varies markedly, the monthly mean albedo estimate is largely affected by the timing of days with small cloud probability.

5. Discussion

This study demonstrates the use of cloud probability information for surface albedo retrieval. At the time of the study only one month of cloud probability data was available globally. In June the northern hemisphere is covered best, but high southern

hemisphere latitudes, mainly Antarctica are missing, because of the low solar zenith angle values. As the cloud cover varies seasonally, it would be desirable to update the parameter values of this study (Table 1 and the form of Eq.12) using global cloud probability data of one year. However, despite of the rather limited cloud probability statistics of this study, the achieved estimation accuracy of monthly means of albedo was satisfactory and the values were in line with the *in situ* measurements.

5

Typically the surface albedo of snow-free surfaces depends on the solar zenith angle such that the minimum is obtained at midday and the albedo is azimuthally symmetric (Briegleb and Ramanathan, 1982; Briegleb et al, 1986; Yang et al., 2008; Manninen et al., 2020). Also for snow outside the melting season the dependence is similar, unless the surroundings are very anisotropic. If the whole diurnal albedo distribution were available using satellite data, it might be a good idea to take that into account in the simulations and deriving the parameter values to be used for albedo estimation (Table 1). However, a satellite based AVHRR instrument observes a site typically only once per day and about at the same time on successive days. Hence, using a Gaussian albedo distribution as a basis for the simulations seemed reasonable.

10

15 For comparison to the approach of this study, surface albedo was estimated also using a standard cloud masking procedure. Then the monthly mean albedo was directly the average value of cloud-free masked pixels, but also here we restricted the processing to cases with *CP* < 20%. The results are shown in Figure 7. Obviously, using the cloud mask one would typically get slightly higher albedo values for snow-free areas than when using the cloud probability values and lower albedo values for snow-covered areas (Greenland Summit, Syowa and Neumayer). This is exactly how cloudiness would affect the albedo retrieval (Section 3.1.1) and supports the notion that the *CP* based approach of this study can exclude the effect of cloud contamination of the TOA reflectance values more effectively than plain cloud mask usage. In addition, the difference between the estimates of the two methods is typically largest for snow-covered areas, where cloud discrimination is very challenging, especially when the sun elevation is low (Karlsson and Håkansson, 2018).

20

25 The largest difference between the two approaches in Cabauw took place in November 2008, when there were only three points available matching the *in situ* measurement times, due to the low solar elevation, and the satellite-based albedo estimate varied in the range 20.6% - 43.3%. The largest value was masked cloud-free, but the *CP* value was 19.8% and the high reflectivity may as well be due to patchy snow or partial cloud contamination. Snow might also explain the fraction of cloud masked pixels with very small *CP* values.

30

The CLARA-A3 SAL will be derived using the *CP* values instead of the binary cloud mask. The pentad means will be derived technically similarly as the monthly means using pentad distributions of *CP*. Future studies of the CLARA-A3 *CP* and cloud mask characteristics will show whether it would be desirable to use both the cloud mask and the *CP* values as the basis for

SAL estimation. In addition, the parameter values to be used in Eqs. 10 and 12 would benefit from an updated analysis, using *CP* data for a whole year as input.

Since the surface albedo is directly related to the TOA reflectance value, the approach presented here for surface albedo
5   estimation could be adapted also to estimating other reflectance-associated surface parameters instead of using the traditional cloud masking, when a time window containing several images is of interest. Naturally, in general the reliability of the method increases with increasing number of points to be averaged.

6.   Conclusions

Cloud probability values to be provided by the CM SAF CLARA-A3 data record offer a good alternative to binary cloud
10   masking for surface reflectance and albedo estimation, when the goal is not in studying individual images, but statistics within a time window. Simple weighted averaging on the basis of the cloud probability values and a basic linear regression correction for biased no clear-sky events containing time windows provide good estimates for surface albedo.

20   **Code availability**

No special code to deliver, only very basic calculations carried out using Mathematica.
Data availability

The cloud probability data used was a test set of a fundamental data record to be published by CM SAF.

25

Author contribution

TM, EJ and NS carried out the theoretical development. TM made the simulations and albedo quality analysis. AR provided *in situ* data and participated in the albedo quality analysis. KGK developed and provided the cloud probability data and related information used in the study. Everybody participated in writing the manuscript.

30

Competing interests

The authors declare that they have no conflict of interest.

References

Anttila, K., Manninen, T., Jääskeläinen, E., Riihelä, A. and Lahtinen, P.: The Role of Climate and Land Use in the Changes in Surface Albedo Prior to Snow Melt and the Timing of Melt Season of Seasonal Snow in Northern Land Areas of 40°N–80°N during 1982–2015, Remote Sens. 10, 1619, https://doi.org/10.3390/rs10101619, 2018.

Augustine, J.: Basic measurements of radiation at station Desert Rock (2008-11). NOAA - Air Resources Laboratory, Boulder, PANGAEA, https://doi.org/10.1594/PANGAEA.719888, 2009a.

Augustine, J.: Basic measurements of radiation at station Desert Rock (2009-04). NOAA - Air Resources Laboratory, Boulder, PANGAEA, https://doi.org/10.1594/PANGAEA.719908, 2009b.

Augustine, J.: Basic measurements of radiation at station Fort Peck (2008-11). NOAA - Air Resources Laboratory, Boulder, PANGAEA, , 2009c.

Augustine, J.: Basic measurements of radiation at station Fort Peck (2009-04). NOAA - Air Resources Laboratory, Boulder, PANGAEA, , 2009d.

Augustine, J.: Basic measurements of radiation at station Desert Rock (2018-07). NOAA - Air Resources Laboratory, Boulder, PANGAEA, , 2019a.

Augustine, J.: Basic measurements of radiation at station Fort Peck (2018-07). NOAA - Air Resources Laboratory, Boulder, PANGAEA, , 2019b.

Briegleb, B., and Ramanathan, V.: Spectral and diurnal variations in clear sky planetary albedo, J. Appl. Meteor., 21, 1160–1171, https://doi.org/10.1175/1520-0450(1982)021,1160:SADVIC.2.0.CO;2, 1982.

Briegleb, B., Minnis, P., Ramanathan, V. and Harrison, E.: Comparison of regional clear-sky albedos inferred from satellite observations and model computations, J. Climate Appl. Meteor., 25, 214–226, https://doi.org/10.1175/1520-0450(1986)025,0214:CORCSA.2.0.CO;2, 1986.

Brisson, A., Le Borgne, P., Marsouin, A.: Development of algorithms for Surface Solar Irradiance retrieval at O&SI SAF Low and Mid Latitudes, Ocean & Sea Ice SAF Scientific Report, 31p, 1999.

Devasthale, A., Raspaud, M., Schlundt, C., Hanschmann, T., Finkensieper, S., Dybbroe, A., Hörnquist, S., Håkansson, N., Stengel, M., and Karlsson, K.-G.: PyGAC: An open-source, community-driven Python interface to preprocess the nearly 40-year AVHRR Global Area Coverage (GAC) data record, GSICS Quarterly Newsletter, Summer 2017, Special Issue on Re-
5   Processing, 11, https://doi.org/10.7289/V5R78CFR, 2017.

Driemel, A., Augustine, J., Behrens, K., Colle, S., Cox, C., Cuevas-Agulló, E., Denn, F. M., Duprat, T., Fukuda, M., Grobe, H., Haeffelin, M., Hodges, G., Hyett, N., Ijima, O., Kallis, A., Knap, W., Kustov, V., Long, C. N., Longenecker, D., Lupi, A., Maturilli, M., Mimouni, M., Ntsangwane, L., Ogihara, H., Olano, X., Olefs, M., Omori, M., Passamani, L., Pereira, E. B.,
10   Schmithüsen, H., Schumacher, S., Sieger, R., Tamlyn, J., Vogt, R., Vuilleumier, L., Xia, X., Ohmura, A., and König-Langlo, G.: Baseline Surface Radiation Network (BSRN): structure and data description (1992–2017), Earth Syst. Sci. Data, 10, 1491-1501, doi:10.5194/essd-10-1491-2018, 2018.

Dybbroe, A., Thoss, A., and Karlsson, K.-G.: NWCSAF AVHRR cloud detection and analysis using dynamic thresholds and
15   radiative transfer modelling – Part I: Algorithm description, J. Appl. Meteorol., 44, 39–54, 2005.

EUMETSAT Ocean and Sea Ice Satellite Application Facility, Global sea ice concentration interim climate data record 2016-onwards (v2.0, 2017), OSI-430-b, (Data extracted from OSI SAF FTP server/EUMETSAT Data Center : 2018-06, NH, accessed 22.4.2021.

20

GCOS, The Global Observing System for Climate: Implementation Needs. Reference Number GCOS-200, 2016.

Hansen, MC, Defries, RS, Townshend, JRG, Sohlberg, R.: Global land cover classification at 1km spatial resolution using a classification tree approach, International Journal of Remote Sensing, 21(7-Jun), 1331-1364, 2000.

25

Heidinger, A.K., Anne, V.R. and Dean, C.: Using MODIS to Estimate Cloud Contamination of the AVHRR Data Record, Journal of Atmospheric and Oceanic Technology, 19, 586 – 601, 2002.

Heidinger, A. K., Straka, W. C., Molling, C. C., Sullivan, J. T., and Wu, X. Q.: Deriving an inter-sensor consistent calibration
30   for   the   AVHRR   solar   reflectance   data   record,   Int.   J.   Remote   Sens.,   31,   6493–6517, https://doi.org/10.1080/01431161.2010.496472, 2010.

Hersbach, H, Bell, B, Berrisford, P, et al.: The ERA5 global reanalysis. Q J R Meteorol Soc. 2020; 146: 1999– 2049. https://doi.org/10.1002/qj.3803

Jääskeläinen, E.; Manninen, T.; Tamminen, J.; Laine, M.: The Aerosol Index and Land Cover Class Based Atmospheric Correction Aerosol Optical Depth Time Series 1982–2014 for the SMAC Algorithm, Remote Sens., 9, 1095. doi:10.3390/rs9111095, 2017.

5

Karlsson, K.-G.; Anttila, K.; Trentmann, J.; Stengel, M.; Meirink, J.F.; Devastale, A.; Hanschmann, T.; Kothe, S.; Jääskeläinen, E.; Sedlar, J.; et al. CLARA-A2: The second edition of the CM SAF cloud and radiation data record from 34 years of global AVHRR data, Atmos. Chem. Phys., 17, 5809–5828, 2017.

10   Karlsson, K.-G.; Johansson, E.; Håkansson, N.; Sedlar, J.; Eliasson, S. Probabilistic Cloud Masking for the Generation of CM SAF Cloud Climate Data Records from AVHRR and SEVIRI Sensors., Remote Sens., 12, 713. https://doi.org/10.3390/rs12040713, 2020.

Karlsson, K.-G.; Devasthale, Abhay.: Inter-Comparison and Evaluation of the Four Longest Satellite-Derived Cloud Climate
15   Data Records: CLARA-A2, ESA Cloud CCI V3, ISCCP-HGM, and PATMOS-x, Remote Sens., 10(10), 1567. https://doi.org/10.3390/rs10101567, 2018.

Karlsson, K.-G. and Håkansson, N.: Characterization of AVHRR global cloud detection sensitivity based on CALIPSO-CALIOP cloud optical thickness information: demonstration of results based on the CM SAF CLARA-A2 climate data record,
20   Atmos. Meas. Tech., 11, 633–649, https://doi.org/10.5194/amt-11-633-2018, 2018.Knap, W.: Basic and other measurements of radiation at station Cabauw (2018-07). Koninklijk Nederlands Meteorologisch Instituut, De Bilt, PANGAEA, https://doi.org/10.1594/PANGAEA.892887, 2018.

Koren, I., and Joseph, J. H.: The histogram of the brightness distribution of clouds in high-resolution remotely sensed images,
25   J. Geophys. Res., 105(D24), 29369– 29377, 2020. doi:10.1029/2000JD900394.

König-Langlo, G,: Basic and other measurements of radiation at Neumayer Station (2008-11). Alfred Wegener Institute, Helmholtz Centre for Polar and Marine Research, Bremerhaven, PANGAEA, https://doi.org/10.1594/PANGAEA.716641, 2009.

30

König-Langlo, G., Sieger, R., Schmithüsen, H., Bücker, A., Richter, F. and Dutton, E.G.: The Baseline Surface RadiationNetwork and its World Radiation Monitoring Centre at the Alfred Wegener Institute. GCOS-174, WCRP Rep. 24/2013, 30 pp., https://bsrn.awi.de/fileadmin/user_upload/bsrn.awi.de/Publications/gcos-174.pdf, 2013.

17

Liang, S.: Narrowband to broadband conversions of land surface albedo: I Algorithms, Remote Sensing of Environment, 76, 213 - 238, 2000.

Liang, S., Shuey, C.J., Russ, A.L., Fang, H., Chen, M., Walthall, C. L., Daughtry, C.S.T. and Hunt, R. Jr.: Narrowband to broadband conversions of land surface albedo: II Validation, Remote Sensing of Environment, 84, 25 - 41, 2002.

Long, C.: Basic measurements of radiation at station Southern Great Plains (2008-11). Argonne National Laboratory, PANGAEA, https://doi.org/10.1594/PANGAEA.724290, 2009a.

Long, C.: Basic measurements of radiation at station Southern Great Plains (2009-04). Argonne National Laboratory, PANGAEA, https://doi.org/10.1594/PANGAEA.724300, 2009b.

Lucht, W., Schaaf, C. B. and Strahler, A. H.: An algorithm for the retrieval of Albedo from space using semiempirical BRDF models. IEEE Trans. Geosci. Remote Sens., 38, 977–998, https://doi.org/10.1109/36.841980, 2000.

Manninen, T., Siljamo, N., Poutiainen, J., Vuilleumier, L., Bosveld, F. and Gratzki, A.: Cloud statistics based estimation of land surface albedo from AVHRR data, Proc. of SPIE, Remote Sensing of Clouds and the Atmosphere IX, Gran Canaria, Spain, 13-15 September 2004, 5571, 412 – 423, 2004.

Manninen, T., Andersson, K. and Riihelä, A., 2011: "Topography correction of the CM-SAF surface albedo product SAL ", Proc. 2011 EUMETSAT Meteorological Satellite Conference, Oslo, CD, 8p.

Manninen, T., Anttila, K., Jääskeläinen, E., Riihelä, A., Peltoniemi, J., Räisänen, P., Lahtinen, P., Siljamo, N., Thölix, L., Meinander, O., Kontu, A., Suokanerva, H., Pirazzini, R., Suomalainen, J., Hakala, T., Kaasalainen, S., Kaartinen, H., Kukko, A., Hautecoeur, O. and Roujean, J.-L.: Effect of small-scale snow surface roughness on snow albedo and reflectance, The Cryosphere, 15, 793–820, https://doi.org/10.5194/tc-15-793-2021, 2021.

Manninen, T., Jääskeläinen, E. and Riihelä, A.: Black and White-Sky Albedo Values of Snow: In Situ Relationships for AVHRR-Based Estimation Using CLARA-A2 SAL, Canadian Journal of Remote Sensing, 18 p., DOI: 10.1080/07038992.2019.1632177, 2019.

Manninen, T., Jääskeläinen, E. and Riihelä, A.: Diurnal Black-Sky Surface Albedo Parameterization of Snow, Journal of Applied Meteorology and Climatology, 59(9), 1415–1428, DOI: https://doi.org/10.1175/JAMC-D-20-0036.1, 2020.

Mayor, S., Smith, W.L. Jr., Nguyen, L., Alberta, A., Minnis, P., Whitlock, C.H. and Schuster, G.L.: Asymmetry in the Diurnal Variation of Surface Albedo, Proc. of International Geoscience and Remote Sensing Symposium, IGARSS'96, Lincoln, 4, 1911 – 1913, 1996.

5 Pirazzini, R.,: Surface albedo measurements over Antarctic sites in summer. J. Geophys. Res., 109, D20118, https://doi.org/10.1029/2004JD004617, 2004.

Proud, S.R., Rasmussen, M.O., Fensholt, R., Sandholt, I., Shisanya, C., Mutero, W., Mbow, C., and Anyamba, A.: Improving the SMAC atmospheric correction code by analysis of Meteosat Second Generation NDVI and surface reflectance data,
10 Remote Sensing of Environment, 114 (8). 1687–1698, doi:10.1016/j.rse.2010.02.020, 2010.

Rahman, H. and Dedieu, G.: SMAC: a simplified method for the atmospheric correction of satellite measurements in the solar spectrum, International Journal of Remote Sensing, 15, 123 – 143, doi:10.3390/rs9111095, 1994.

15 Riihelä, A.; Manninen, T.; Laine, V.; Andersson, K.; Kaspar, F. CLARA-SAL: A global 28 yr timeseries of Earth's black-sky surface albedo, Atmos. Chem. Phys., 13, 3743–3762, 2013.

Riihelä, A., Manninen, T., Laine, V., Andersson, K., & Kaspar, F.. CLARA-SAL: A global 28 yr timeseries of Earth's black-sky surface albedo, Atmospheric Chemistry and Physics, 13(7), 3743-3762, 2013.
20
Román, M. O., Schaaf, C.B., Lewis, P., Gao, F., Anderson, G.P., Privette, J.L. Strahler, A.H., Woodcock, C.E. and Barnsley, M.: Assessing the coupling between surface albedo derived from MODIS and the fraction of diffuse skylight over spatially-characterized landscapes, Remote Sens. Environ., 114, 738–760, https://doi.org/10.1016/j.rse.2009.11.014, 2010.

25 Roujean, J.-L., Leroy, M. and Deschamps, P.-Y.: A Bidirectional Reflectance Model of the Earth's Surface for the Correction of Remote Sensing Data, Journal of Geophysical Research, 97, D18, 20455 – 20468, 1992.

Schulz, J., Albert, P., Behr, H.-D., Caprion, D., Deneke, H., Dewitte, S., Dürr, B., Fuchs, P., Gratzki, A., Hechler, P., Hollmann, R., Johnston, S., Karlsson, K.-G., Manninen, T., Müller, R., Reuter, M., Riihelä, A., Roebeling, R., Selbach, N., Tetzlaff, A.,
30 Thomas, W., Werscheck, M., Wolters, E., and Zelenka, A.: Operational climate monitoring from space: the EUMETSAT Satellite Application Facility on Climate Monitoring (CM SAF), Atmos. Chem. Phys., 9, 1687–1709, https://doi.org/10.5194/acp-9-1687-2009, 2009.

Steffen, K., J. E. Box, and W. Abdalati, 1996 "Greenland Climate Network: GC-Net", in Colbeck, S. C. Ed. CRREL 96-27 Special Report on Glaciers, Ice Sheets and Volcanoes, trib. to M. Meier, pp. 98-103.

5   Vuilleumier, L.: Basic and other measurements of radiation at station Payerne (2008-11). Swiss Meteorological Agency, Payerne, PANGAEA, https://doi.org/10.1594/PANGAEA.735084, 2010a.

Vuilleumier, L.: Basic and other measurements of radiation at station Payerne (2009-04). Swiss Meteorological Agency, Payerne, PANGAEA, https://doi.org/10.1594/PANGAEA.735299, 2010b.

10   Vuilleumier, L.: Basic and other measurements of radiation at station Payerne (2018-07). Swiss Meteorological Agency, Payerne, PANGAEA, https://doi.org/10.1594/PANGAEA.898990, 2019.

Wu, A., Li, Z. and Cihlar, J.: Effects of land cover type and greenness on advanced very high resolution radiometer bidirectional reflectances: Analysis and removal, Journal of Geophysical Research, 100, D5, 9179 - 9192 , 1995.

15

Yamanouchi, T.: Basic and other measurements of radiation at station Syowa (2008-11). National Institute of Polar Research, Tokyo, PANGAEA, https://doi.org/10.1594/PANGAEA.741002, 2010.

Yang, F., Mitchell, K., Hou, Y.-T., Dai, Y., Zeng, X., Wang, Z. and Liang, X.-Z.: Dependence of land surface albedo on solar
20   zenith angle: Observations and model parameterization, J. Appl. Meteor. Climatol., 47, 2963–2982, https://doi.org/ 10.1175/2008JAMC1843.1, 2008.

Appendix: Used parameter symbols

Symbol	Meaning
c_1	Empirical coefficient used in final albedo estimate retrieval
c_2	Empirical coefficient used in final albedo estimate retrieval
CP	Cloud probability
$\overline{CP}$	Monthly mean cloud probability
d	Weight parameter for albedo monthly mean retrieval
$f(\alpha)$	Albedo distribution
$f_c(\alpha)$	Probability density function of albedo for cloudy pixels
$f_{CP}(CP)$	Pixelwise cloud probability density function
$f_k(k)$	Cloud distribution based on cloud fraction
$f_p(p)$	Probability density function of shadows
$f_s(\alpha)$	Probability density function of albedo for possibly shaded pixels
$f_{Sc}(\alpha)$	Satellite based probability density function of albedo for cloudy pixels
$f_{Ss}(\alpha)$	Satellite based probability density function of albedo for possibly shaded pixels
$f_{St}(\alpha)$	Satellite based total probability density function of albedo
$f_t(\alpha)$	Total probability density function of albedo
k	Cloud fraction
p	Probability of shadow
α	Albedo
$\bar{\alpha}$	Monthly mean albedo, first estimate
$\hat{\alpha}$	Monthly mean albedo, final estimate
β	Kurtosis
γ	Skewness
σ	Standard deviation

5

Tables

Table 1. Parameter values of Eq. 10 for monthly mean, standard deviation, skewness and kurtosis of surface albedo.

Variable	c_1	c_2
Mean	0.006343	-0.1335
Standard deviation	-0.0005595	-0.04121
Skewness	0.008168	0.05647
Kurtosis	0.001205	0.1137

Table 2. Simulated statistics for the absolute and relative differences of the estimated (^) and true values of albedo (α), standard deviation (σ) skewness (γ) and kurtosis (β). The calculations were made for albedo values 10%, 20%, 30%, 40%, 50%, 60%, 70% and 80%. The albedo values are in the range 0 – 100%.

	$|\hat{\alpha}-\alpha|$	$\dfrac{|\hat{\alpha}-\alpha|}{\alpha}$	$|\hat{\sigma}-\sigma|$	$\dfrac{|\hat{\sigma}-\sigma|}{\sigma}$	$|\hat{\gamma}-\gamma|$	$\dfrac{|\hat{\gamma}-\gamma|}{\gamma}$	$|\hat{\beta}-\beta|$	$\dfrac{|\hat{\beta}-\beta|}{\beta}$
Mean	0.48	0.011	0.0079	0.0076	0.038	0.0098	0.0033	0.018
Median	0.32	0.0089	0.0063	0.0041	0.020	0.0056	0.0018	0.010
90 % quantile	1.1	0.022	0.019	0.018	0.09	0.022	0.0083	0.042
Max	2.8	0.078	0.037	0.058	0.30	0.071	0.035	0.124

5

Table 3. Monthly mean black-sky surface albedo values based on AVHRR reflectance and *CP* values and the monthly means values of the corresponding times of *in situ* surface albedo measurements for several BSRN *in situ* sites (König-Langlo et el., 2013; Driemel et al., 2018): Desert Rock (Augustine, 2009a, 2009b, 2019a), Fort Peck (Augustine, 2009c, 2009d, 2019b), Payerne (Vuilleumier, 2010a, 2010b, 2019), Southern Great Plains (Long, 2009a, 2009b), Cabauw (Knap, 2018), Syowa (Yamanouchi, 2010) and Neumayer Station (König-Langlo, 2009). Date from the Greenland Summit *in situ* site is also included (Steffen et al., 1996). The number of observations included in the mean value are given as well as the mean distance of the satellite pixels from the *in situ* measurement mast.

Site	Location	Time	Number of observations	Mean distance [km]	In situ albedo [%]	AVHRR based black-sky albedo [%]	Albedo difference in situ - AVHRR [%]
Desert Rock	36.626°N, 116.018°W	November 2008	69	3.0	21.5	20.3	1.2
		April 2009	120	3.1	20.7	20.0	0.7
		July 2018	124	2.6	20.7	21.0	-0.3
Fort Peck	48.31°N, 105.1°W	November 2008	19	3.1	18.8	15.8	3.0
		April 2009	90	2.9	17.3	15.2	2.1
		July 2018	177	2.7	16.2	17.4	-1.2
Payerne	46.815°N, 6.944°E	November 2008	17	3.2	24.6	17.6	7.0
		April 2009	124	3.1	23.3	21.3	2.0
		July 2018	151	2.5	21.6	19.8	1.8
Southern Great Plains	36.605°N, 97.485°W	November 2008	65	2.0	20.9	19.3	1.6
		April 2009	77	2.9	20.2	20.2	0.0
Cabauw	51.971°N, 4.927°E	July 2018	171	2.9	23.0	19.7	3.3
Syowa	69.005°S, 39.589°E	November 2008	63	2.9	81.3	80.7	0.6
Neumayer Station	70.65°S, 8.25°W	November 2008	80	2.6	82.3	82.8	-0.5
Greenland Summit	72.580°N, 38.500°W	April 2009	79	3.1	84.4	85.4	-1.0

Figure captions

Figure 1. Left: The median (solid line) and the 80% variation range (grey shaded area) of the pixelwise cloud probability distributions for June 2012. Every 5th *CP* end product pixel (0.25° x 0.25°) available globally is included in the statistics. The frequencies are scaled with the median value at *CP* = 0%. Right: Ten largest pixelwise relative cloud probability distributions and the mean (dashed curve) of all *CP* distributions scaled with its maximum value. The solar zenith angle is restricted to not exceed 70°.

Figure 2. The flow diagram of estimating cloud-free monthly mean surface albedo values in pixel basis starting from the TOA reflectance and *CP* values of the month in question.

Figure 3. Examples of simulated cloudy albedo distributions for diverse values of parameters *b* (blue shades) and *c* (diverse values of dashing) in Eq. 5. The example surface albedo values are assumed to be Gaussian with mean values 20% (top left), 50% (top right) and 80% (top bottom) and a standard deviation of 2%. The surface albedo mean is shown as a red line and the distribution as a yellow curve. The parameter *p* in Eq. 4 had a random value in the range [0,1]. The example cloud albedo value is assumed to be Gaussian with a mean of 60% and standard deviation of 20%.

Figure 4. The relationship between the number of points in the cloud distribution and the simulated mean (left) and relative mean (right) albedo accuracy.
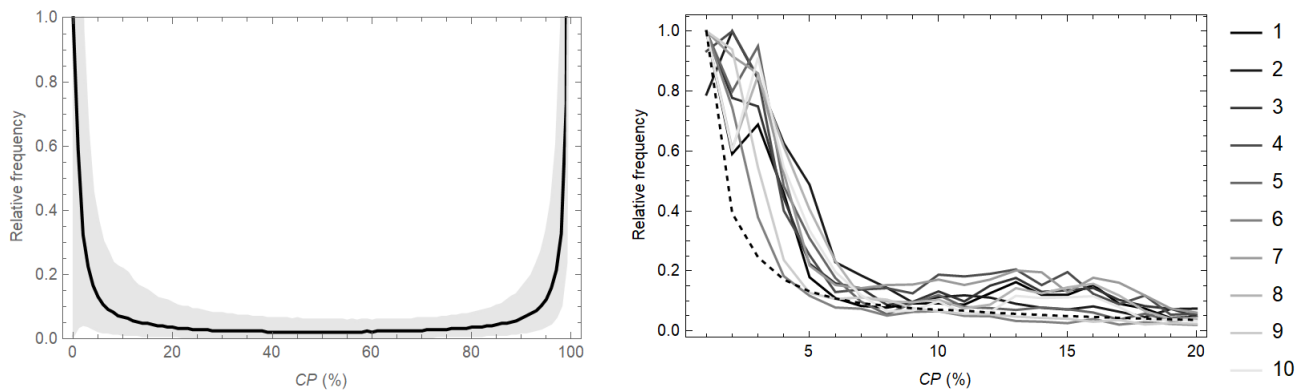
Figure 5. The albedo retrieval distributions at Desert Rock, Payerne and Southern Great Plains in April 2009 and Syowa in November 2008. The cloud probability values of the individual black-sky satellite based estimates are indicated by the colours. The monthly mean estimate is shown in red line.

Figure 6. The albedo retrieval distributions at Arctic Ocean (73.370°N, 139.180°W), Kara Sea (2.680°N, 62.860°E) and Laptev Sea (75.320°N, 125.720°E) in April 2009 and July 2018. The cloud probability values of the individual black-sky satellite based estimates are indicated by the colours. The monthly mean estimate is shown in red dashed line.

Figure 7. The difference between the monthly mean surface albedo estimates derived using the cloud masking (CM) and cloud probability (CP) approaches for several Northern hemisphere test sites in July 1979, April 1981, November 2008, April 2009, July 2018 and April 2020. For Greenland Summit no satellite albedo data was available for November 2008 due to low solar elevation. For the Southern hemisphere sites Syowa and Neumayer Station data was available for January 1979 and November 2008.

Figure 1. Left: The median (solid line) and the 80% variation range (grey shaded area) of the pixelwise cloud probability distributions for June 2012. Every 5th CP end product pixel (0.25° x 0.25°) available globally is included in the statistics. The frequencies are scaled with the median value at $CP = 0\%$. Right: Ten largest pixelwise relative cloud probability distributions and the mean (dashed curve) of all CP distributions scaled with its maximum value. The solar zenith angle is restricted to not exceed 70°.
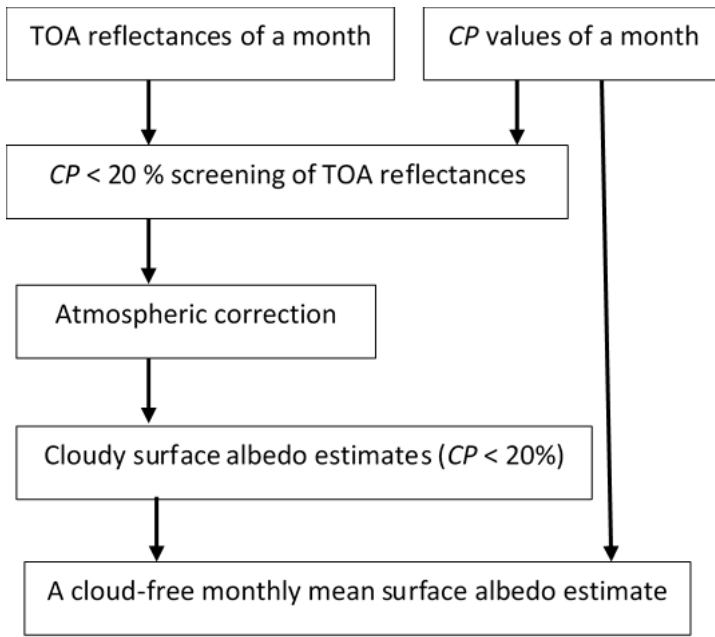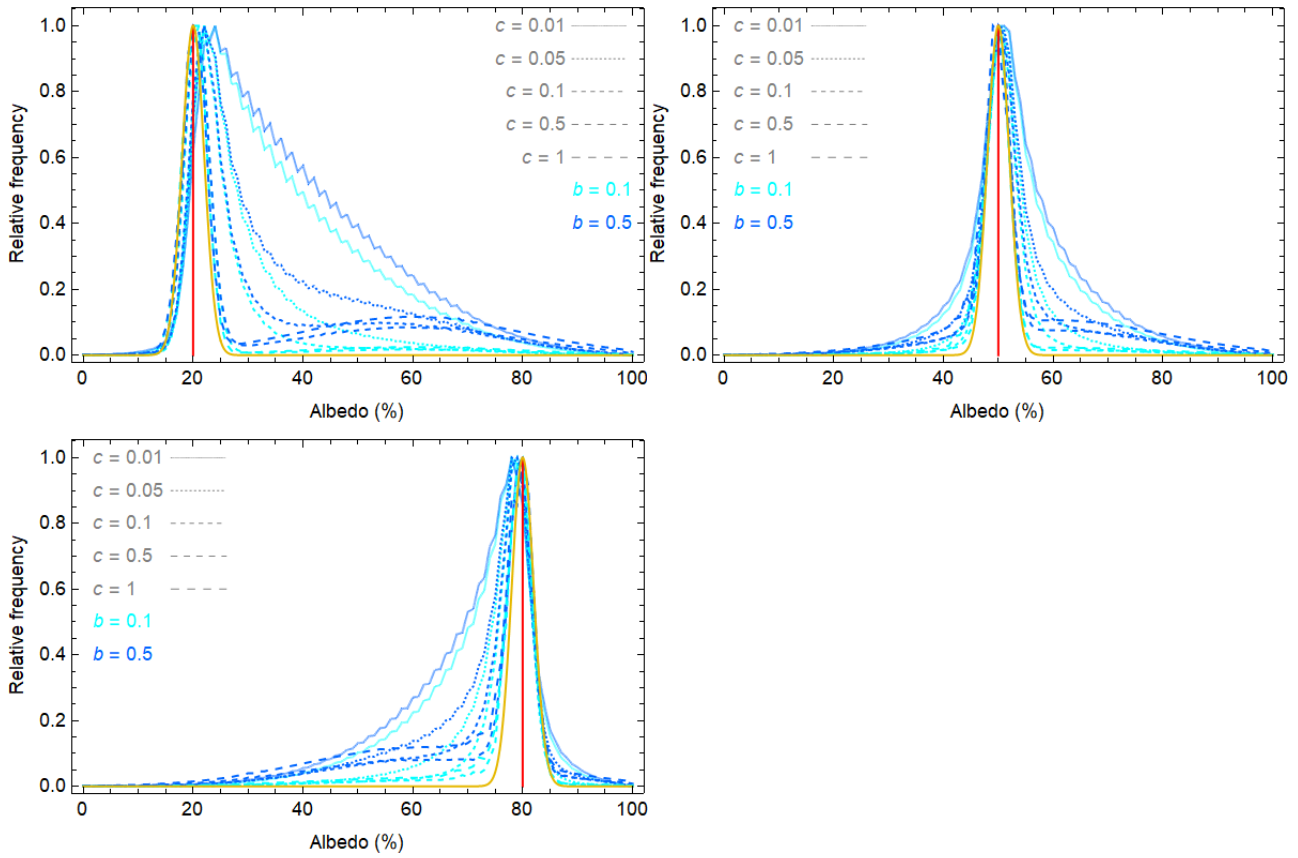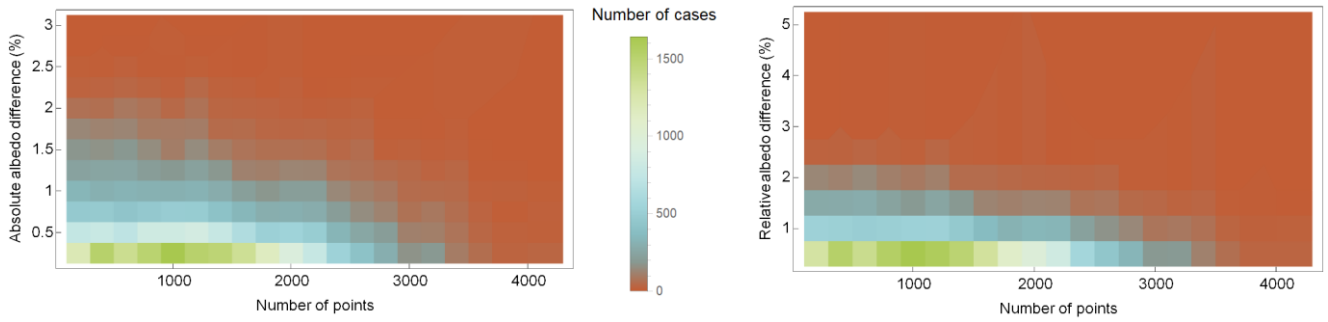
Figure 2. The flow diagram of estimating cloud-free monthly mean surface albedo values in pixel basis starting from the TOA reflectance and *CP* values of the month in question.
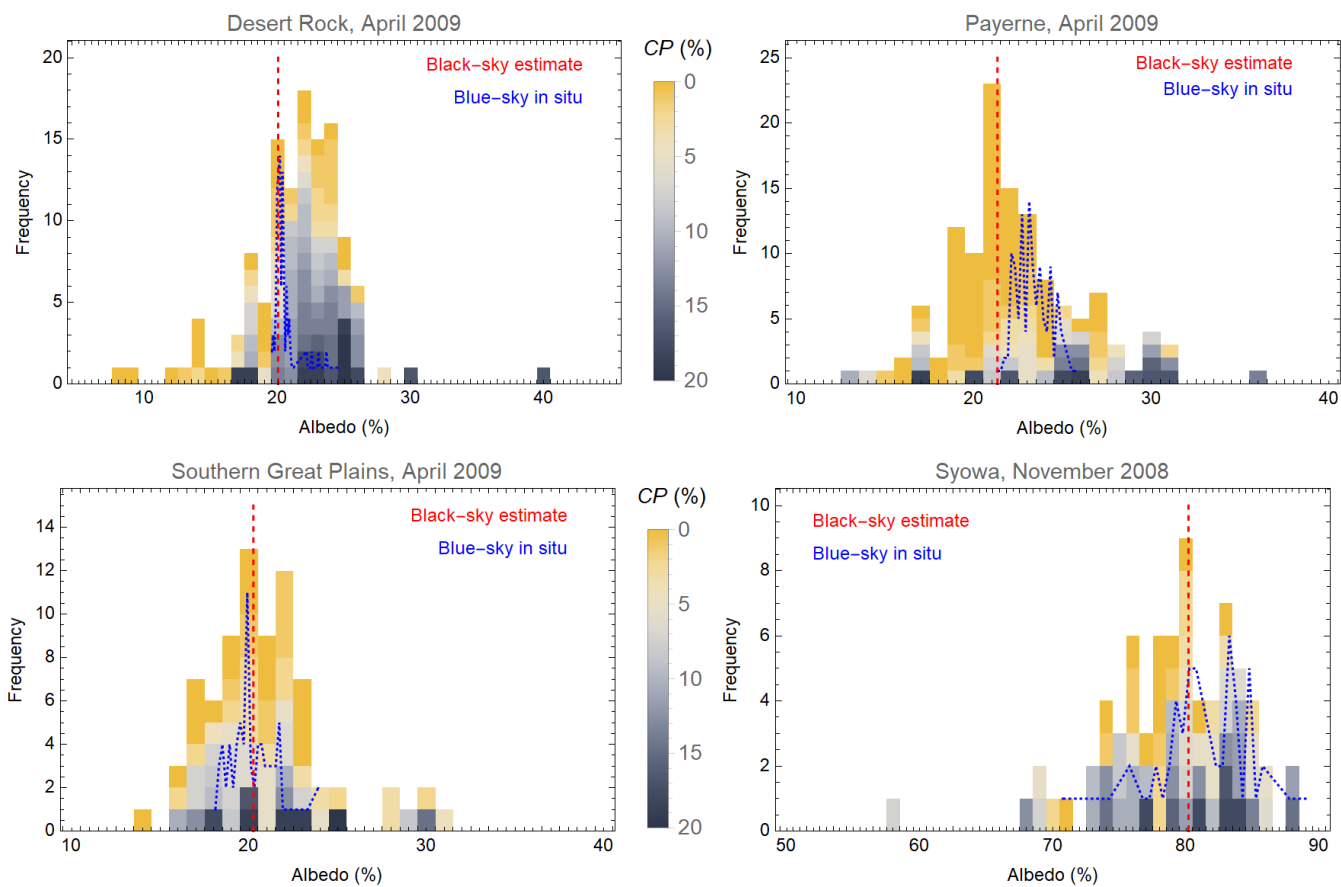
5

Figure 3. Examples of simulated cloudy albedo distributions for diverse values of parameters b (blue shades) and c (diverse values of dashing) in Eq. 5. The example surface albedo values are assumed to be Gaussian with mean values 20% (top left), 50% (top right) and 80% (top bottom) and a standard deviation of 2%. The surface albedo mean is shown as a red line and the distribution as a yellow curve. The parameter p in Eq. 4 had a random value in the range [0,1]. The example cloud albedo value is assumed to be Gaussian with a mean of 60% and standard deviation of 20%.
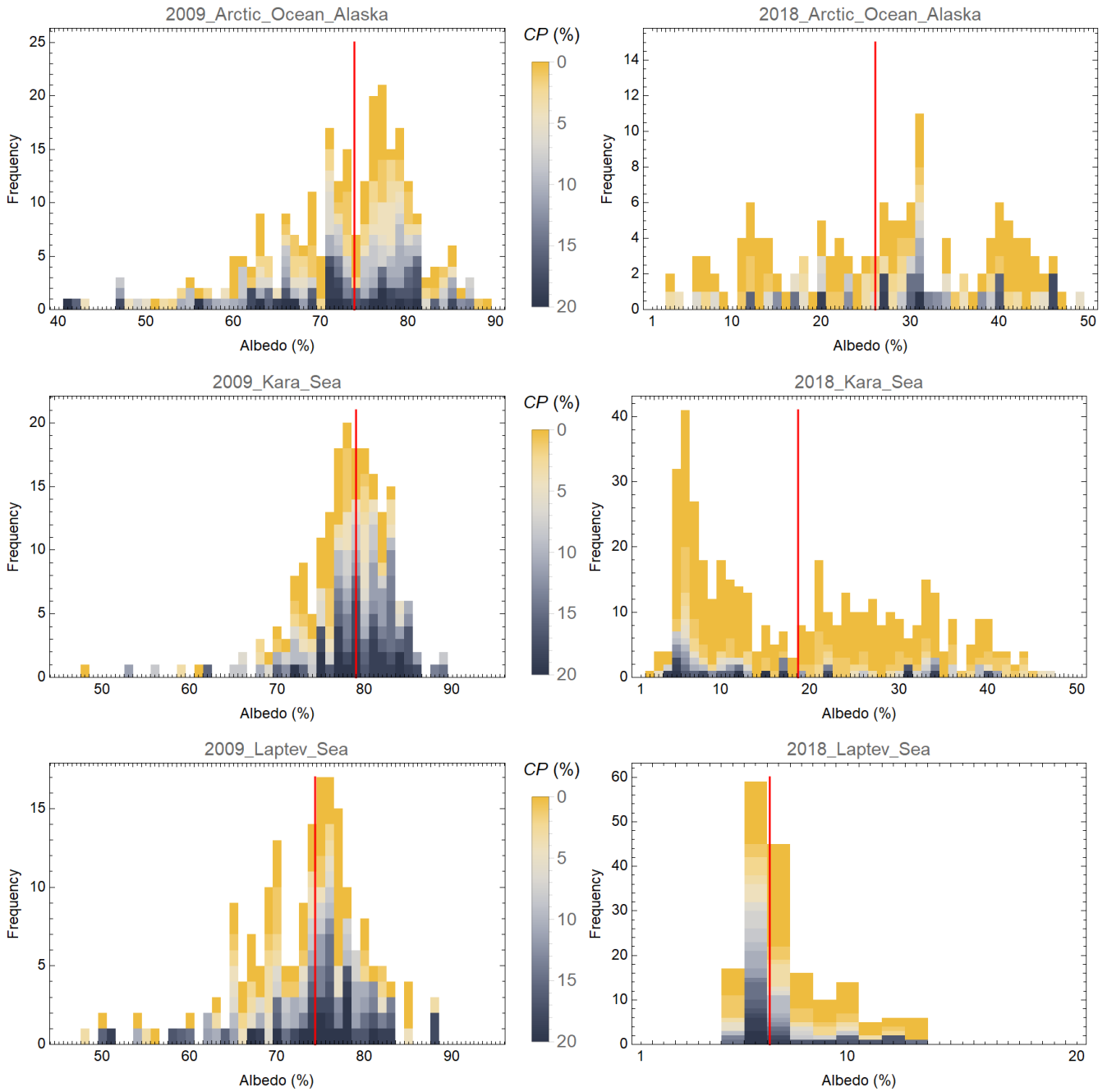
Figure 4. The relationship between the number of points in the cloud distribution and the simulated mean (left) and relative mean (right) albedo accuracy.

5 Figure 5. The albedo retrieval distributions at Desert Rock, Payerne and Southern Great Plains in April 2009 and Syowa in November 2008.

5   Figure 6. The albedo retrieval distributions at Arctic Ocean (73.370°N, 139.180°W), Kara Sea (2.680°N, 62.860°E) and Laptev Sea (75.320°N, 125.720°E) in April 2009 and July 2018. The cloud probability values of the individual black-sky satellite based estimates are indicated by the colours. The monthly mean estimate is shown in red dashed line.

Figure 7. The difference between the monthly mean surface albedo estimates derived using the cloud masking (CM) and
5   cloud probability (CP) approaches for several Northern hemisphere test sites in July 1979, April 1981, November 2008,
April 2009, July 2018 and April 2020. For Greenland Summit no satellite albedo data was available for November 2008 due
to low solar elevation. For the Southern hemisphere sites Syowa and Neumayer Station data was available for January 1979
and November 2008.